

Simulation of GaN and AlGa_N static induction transistors

Emre Alptekin, Ozgur Aktas *

Department of Electrical and Electronics Engineering, Bilkent University, 06800 Ankara, Turkey

Received 7 April 2005; received in revised form 7 February 2006; accepted 13 March 2006

Available online 12 May 2006

The review of this paper was arranged by Prof. S. Cristoloveanu

Abstract

GaN and AlGa_N static induction transistors (SITs) are simulated using a two-dimensional self-consistent drift-diffusion simulator incorporating impact-ionization and self-heating effects. The results indicate that GaN SIT devices can have performance comparable to SiC SITs. As compared to GaN SITs, AlGa_N SITs will have higher breakdown voltage but smaller maximum current. The power per unit gate width obtainable from GaN and AlGa_N SITs are approximately the same, but the maximum power handling capacity of the AlGa_N SIT is significantly higher due to bigger optimum load resistance. A comparison of the characteristics of GaN and AlGa_N SITs with AlGa_N/GaN HEMTs shows that the SIT devices have much lower cut-off frequency and smaller transconductance but can produce higher total output power.

© 2006 Elsevier Ltd. All rights reserved.

Keywords: GaN; High power transistors; Static induction transistor

1. Introduction

Transistors based on GaN and its alloys offer great potential for high-power high-frequency microwave operation. As a result of the intensive research, record power and high-frequency results have been demonstrated for AlGa_N/GaN high-electron-mobility transistors (HEMTs) [1–3]. However, work on GaN based static induction transistors (SITs) has been limited due to the excellent characteristics of AlGa_N/GaN HEMTs and due to the technological difficulties encountered for the fabrication procedure of SITs. Previously, properties of GaN SITs were investigated using two-dimensional simulations [4] and basic SIT operation was demonstrated experimentally [5]. In this work, the properties of GaN and AlGa_N SIT devices are investigated in further detail and using more recent results for the impact ionization coefficients.

Fabrication of SIT devices is difficult since the device geometry is non-planar, requiring Schottky gate contacts on etched surfaces and backside drain contacts. In comparison, AlGa_N/GaN HEMTs enjoy a relatively uncomplicated fabrication procedure. However, for use in high-power circuits, the fabrication procedure of HEMTs is complicated by the need for cooling and by backside via requirements. Procedures such as epitaxial-liftoff have been developed to address some of these issues. Furthermore, AlGa_N/GaN HEMTs with recessed gate structures have been demonstrated using low damage etching techniques. Thus, the techniques developed for fabrication of high power AlGa_N/GaN HEMT will benefit and make feasible the fabrication of SITs based on GaN and its alloys.

Despite the fact that the high-frequency performance of SITs is expected to be not as good as that of HEMTs, the possibility of increased power density, increased power output and larger breakdown voltage is an advantage of the SIT structure. SiC SITs have demonstrated record power levels and record high-voltage operation at useful microwave frequencies [6,7]. This provides a motivation to study the properties of GaN based SITs.

* Corresponding author. Tel.: +90 312 290 3394; fax: +90 312 266 4192.
E-mail address: aktas@ee.bilkent.edu.tr (O. Aktas).

Table 1
Material parameters used in this work, along with the references from which they were taken

	GaN	Al _{0.1} Ga _{0.9} N	Al _{0.2} Ga _{0.8} N
Band gap (eV)	3.47 [9]	3.74 [10]	4 [10]
Thermal conductivity (W/Km)	130 [12]	136.5 [11]	144.1 [11]
V_{esat} (m/s)	1.90×10^5 [15]	1.56×10^5 [15]	1.32×10^5 [15]
m_e	$0.180m_0$ [11]	$0.184m_0$ [13]	$0.188m_0$ [13]
m_h	$1.2m_0$ [15]	$1.4m_0$ [13]	$1.6m_0$ [13]

The relative mass values of Al_xGa_(1-x)N are calculated by harmonic mean of GaN and AlN.

Table 2
Model parameters used in Eq. (2)

	GaN	Al _{0.2} Ga _{0.8} N
u_L (cm ² /V s)	1266.1	356.1
$u_{L\text{exp } T}$	-1.55	-0.95
$u_{L\text{min}}$ (cm ² /V s)	62	122
$u_{L\text{exp } T}$	-1.05	-1.05
C_{ref} (cm ⁻³)	2.0E+019	2.00E+019
$C_{\text{refexp } T}$	6.02	6.02
alpha	0.29	0.29
alpha _{exp T}	0.34	0.34
beta	4.32	5.32
F_{crit} (V/cm)	195552.9	365552.9
v_{sat} (m/s)	1.90E+5	1.32E+005
n_2	0.79	1.04
b_2	3.32	4.32
T_{ref} (K)	300	300
$a_{\text{exp } T}$	-0.19	-0.23
$n_{2\text{exp } T}$	-0.2	-0.5

2. Methodology

The device simulator MINIMOS (version 6.1) was used to investigate the characteristics of GaN and AlGaN SITs [8]. The material parameters corresponding to GaN,

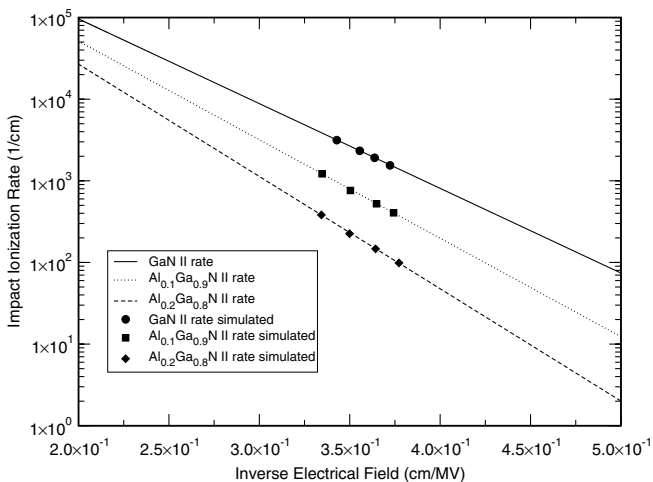


Fig. 1. Impact ionization rates as measured from test simulations and as calculated by the MINIMOS model with the parameters adjusted to reproduce Monte Carlo data.

Al_{0.1}Ga_{0.9}N, and Al_{0.2}Ga_{0.8}N were entered into the material parameter database of MINIMOS. Tables 1 and 2 list the relevant material parameters used, along with the references from which these values were taken [9–15]. In particular, the impact ionization rates reported in [14] were used for the calculations. Fig. 1 shows the impact ionization rates calculated by the MINIMOS model with the parameters set to the values in [14] and the values measured from MINIMOS simulation results.

To enable accurate modeling of the velocity-field characteristics of GaN and AlGaN, the built-in velocity-field-temperature model of MINIMOS-NT was modified to account for the smoother transition from peak velocity to saturation velocity. The formula employed for this purpose is written as

$$u_{LI} = u_{L\text{min}} t^{u_{L\text{exp } T}} + \frac{(u_L - u_{L\text{min}}) t^{u_{L\text{exp } T}}}{1 + \left(\frac{N}{C_{\text{ref}} t^{C_{\text{refexp } T}}} \right)^{\alpha} t^{\alpha_{\text{exp } T}}} \quad \text{where } t = \frac{T}{T_{\text{ref}}} \quad (1)$$

where N is the total doping density, T is the temperature and $u_{L\text{min}}$, T_{ref} , $u_{L\text{exp } T}$, u_L , C_{ref} , $C_{\text{refexp } T}$, α , and $\alpha_{\text{exp } T}$ are the model parameters.

And, the high-field mobility is then modeled as

$$u_{LIF} = \frac{u_{LI} + \frac{v_{\text{sat}} e^{b_2}}{F_{\text{crit}}}}{1 + a(t + 2.2)^{a_{\text{exp } T}} e^{n_2} + e^{\beta a}} \quad \text{where} \quad t = \frac{T}{T_{\text{ref}}} \quad \text{and} \quad e = \frac{E_f}{F_{\text{crit}}} \quad (2)$$

where u_{LI} is the low field mobility as expressed in Eq. (1), v_{sat} is the saturation velocity, E_f is the electrical field, T is the temperature and F_{crit} , T_{ref} , a , $a_{\text{exp } T}$, b_2 , n_2 , and β are the parameters determined by fitting to Monte Carlo simulation data. The low-field mobility model given in Eq. (1) is the same as the mobility model in MINIMOS. In order to achieve better temperature dependence and smoother transition from peak velocity to saturation velocity, the high-field mobility model given in Eq. (2) was modified from the mobility model in Ref. [15]. The parameters in the above models were selected to fit the velocity-field characteristics as calculated by the Monte Carlo program of Ref. [14]. The fit was made for GaN and Al_{0.2}Ga_{0.8}N at 300 K, 600 K, and 1000 K at a doping of $1 \times 10^{18} \text{ cm}^{-3}$. Other parameters were selected to reproduce the variation of velocity-field characteristics as a function of doping based on results from [15]. Table 2 lists the parameters used for the velocity-field model in Eqs. (1) and (2). The mobility value of Al_{0.1}Ga_{0.9}N was determined as the harmonic mean of mobilities of GaN and Al_{0.2}Ga_{0.8}N as

$$\frac{1}{\mu_{\text{Al}_{0.1}\text{Ga}_{0.9}\text{N}}} = \frac{1}{\mu_{\text{GaN}}} + \frac{1}{\mu_{\text{Al}_{0.2}\text{Ga}_{0.8}\text{N}}} \quad (3)$$

In Fig. 2a, the results from the velocity-field model with the parameters listed in Table 2 are compared with the Monte Carlo produced data points for a doping of $1 \times 10^{18} \text{ cm}^{-3}$. In Figs. 2b and 2c, the results from the model and the val-

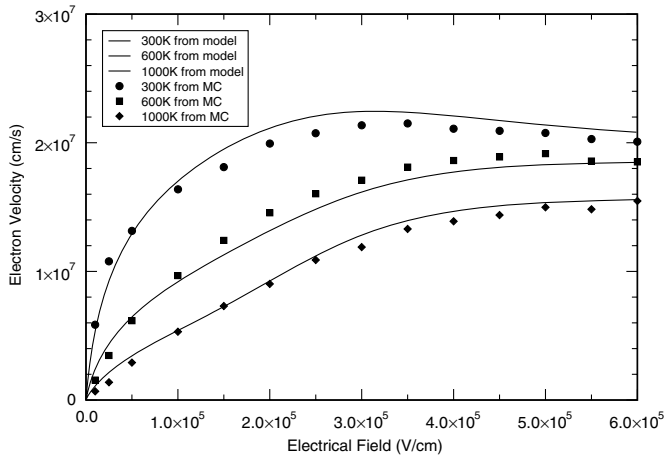


Fig. 2a. Velocity-field characteristics for GaN at a doping of $1 \times 10^{18} \text{ cm}^{-3}$ given by the MINIMOS with the parameters in Table 2 using Eq. (1), and the data points obtained from the non-parabolic multi-valley Monte Carlo program.

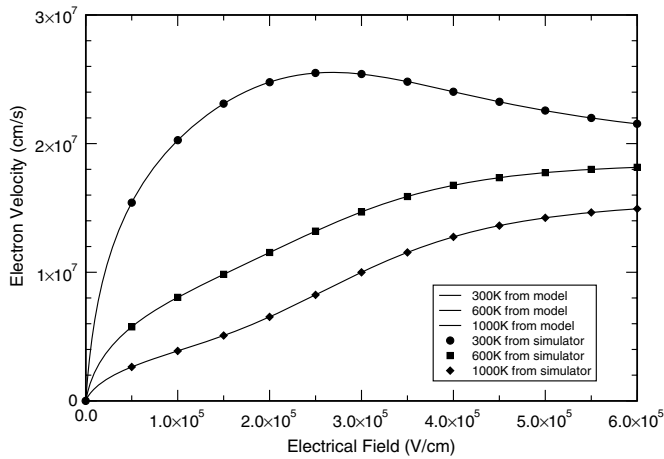


Fig. 2b. Velocity-field characteristics for GaN at different temperatures at a doping of $1 \times 10^{17} \text{ cm}^{-3}$ given by the MINIMOS with the parameters in Table 2 using Eq. (1), and results obtained from test runs on rectangular semiconductor slabs with ohmic contacts on both end.

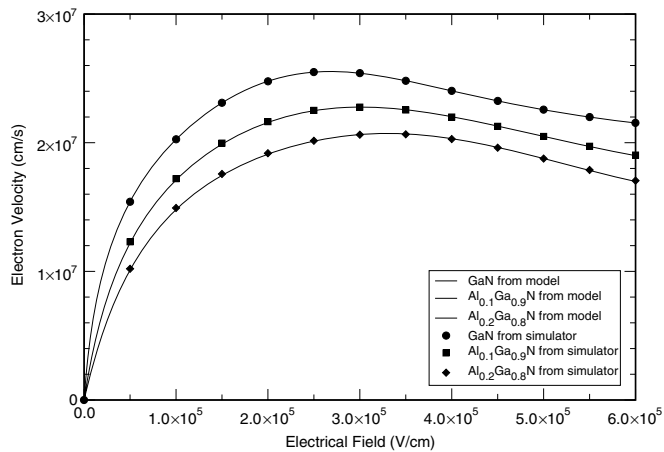


Fig. 2c. Velocity-field characteristics at a doping of $1 \times 10^{17} \text{ cm}^{-3}$ for GaN, $\text{Al}_{0.1}\text{Ga}_{0.9}\text{N}$, and $\text{Al}_{0.2}\text{Ga}_{0.8}\text{N}$ at 300 K given by the MINIMOS with the parameters in Table 2 using Eq. (1), and results obtained from test runs on rectangular semiconductor slabs with ohmic contacts on both end.

ues taken from simulation results are shown to demonstrate that the model is correctly implemented in the simulator. The velocity-field curve for GaN shown in Fig. 2b is similar to that reported in [15]. The change of the velocity-field curves with aluminum mole fraction reflects the assumption made for the alloy scattering potential in [15] and hence is consistent with the impact ionization rates employed.

It needs to be pointed out that, as explained in [15], there is an uncertainty on the impact ionization rates in AlGa_n. The impact ionization rate in AlGa_n is affected by alloy scattering, which also results in the reduction in mobility and other changes in the velocity-field curve. There have been different assumptions about the alloy scattering potential in AlGa_n [14,15]. The values in [14] were calculated by assuming an alloy scattering potential equal to half of the conduction band offsets. If the alloy scattering is weaker, the breakdown voltage and the velocity-field characteristics of AlGa_n will be closer to that of GaN.

The simulated device geometry is shown in Fig. 3. The dimensions of the device were selected to be similar to the values used for SiC and GaN devices [4,7] and a range of values for the source length was investigated. The source-to-gate spacing was adjusted to safely avoid breakdown in this region for the range of gate voltages used in this work. Source and drain sub-contact region (regions indicated by L_{ssub} and L_{dsub}) doping was taken to be $1 \times 10^{18} \text{ cm}^{-3}$, and the rest of the device, including the channel, was assumed to have uniform doping with the values used indicated in the text.

Assuming only backside cooling, the single thermal contact for the device was placed to coincide with the drain contact. The thermal contacts were assumed to have a thermal resistance of $4 \times 10^{-1} \text{ K cm}^2/\text{W}$, which is approximately equal to the thermal resistance of a 2 mm thick copper heat sink. With this assumption, direct-current steady-state or

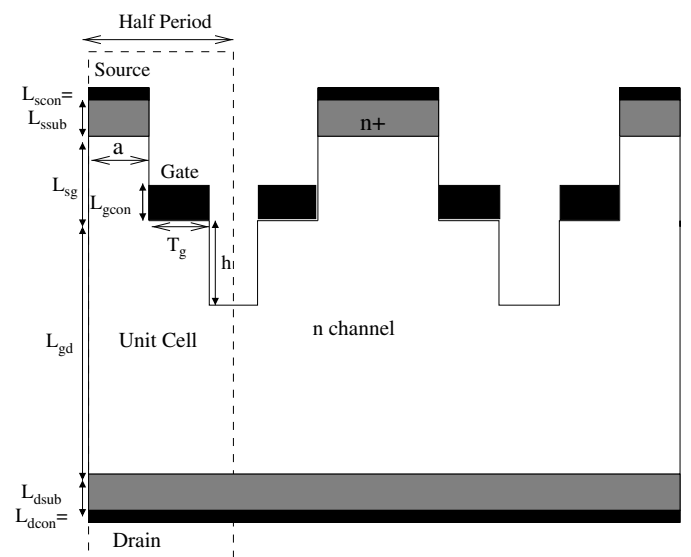


Fig. 3. The device geometry used for the simulations in this work.

RF continuous-wave operation is not possible and the device will have to be pulsed. In order to approximate the average conditions for pulsed operation, the thermal contact resistances and the thermal resistivity of all materials were scaled by a factor corresponding to the duty-cycle. In order to further reduce the power density, the half-period of the device was selected to be much larger than the gate length. To reduce the parasitic capacitances, the gate metal was assumed not to cover the trench completely. To avoid breakdown at the gate corner, the areas of the trench that is not covered by the gate metallization was assumed to be further etched down by h micrometers resulting in the structure shown in Fig. 3. The maximum temperature allowable in the device was set to 1000 K and the simulations were aborted if this value is reached.

At high fields, impact ionization in the device results in breakdown. The state of breakdown was identified by observing the difference in the drain-current between simulations with the impact-ionization model turned off and simulations with the impact-ionization model turned on, and the breakdown was assumed to have set in when the difference increased to 5%.

3. Results

The current–voltage characteristics of the GaN and AlGaIn SITs with a channel doping of $1 \times 10^{17} \text{ cm}^{-3}$ were simulated by employing dimensions listed in Table 3 and by using the thermal model with the scaling that approximates a 5% duty-cycle. The impact ionization and self-heating effects were included as described before. The results are compared in Figs. 4a–4c for the GaN, $\text{Al}_{0.1}\text{Ga}_{0.9}\text{N}$, and $\text{Al}_{0.2}\text{Ga}_{0.8}\text{N}$ SITs, respectively. Fig. 4d shows the current voltage characteristic of the GaN SIT at a fixed temperature of 300 K.

3.1. Thermal analysis

In Fig. 4a, pronounced self-heating effects are observed. Comparison with Fig. 4d shows that the self-heating results in significantly decreased current as expected from the variation of the velocity-field characteristics with temperature.

Table 3
Dimensions employed in the simulations for the device geometry shown in Fig. 3

a	0.25
Half-period	5.25
L_{scon}	0.2
L_{ssub}	0.4
L_{sg}	0.9
h	1.0
L_{gd}	2.6
L_{dsub}	0.4
L_{dcon}	0.2
L_{gcon}	0.4
T_{g}	0.5

The dimensions given are in micrometers.

In addition, self-heating results in a change of the differential resistance of the $I_{\text{DS}}-V_{\text{DS}}$ curves in the saturated region from the value observed in Fig. 4d, in particular, to the negative-differential resistance observed for large I_{DS} in Figs. 4a–4c. For the GaN SIT simulated at $V_{\text{GS}} = 0$, the maximum device temperature increases from 322 K to 778 K as V_{DS} increases from 4 V to 100 V resulting in the negative differential resistance. As expected, the reduction of the drain-current due to self-heating is less severe for smaller values of gate-bias.

With the thermal model parameters set for 5% duty-cycle, the maximum temperatures in the devices at the bias condition for maximum current at zero gate-bias are 362 K, 402 K, and 430 K for the GaN, $\text{Al}_{0.1}\text{Ga}_{0.9}\text{N}$, and $\text{Al}_{0.2}\text{Ga}_{0.8}\text{N}$ SITs, respectively. The increase in temperature

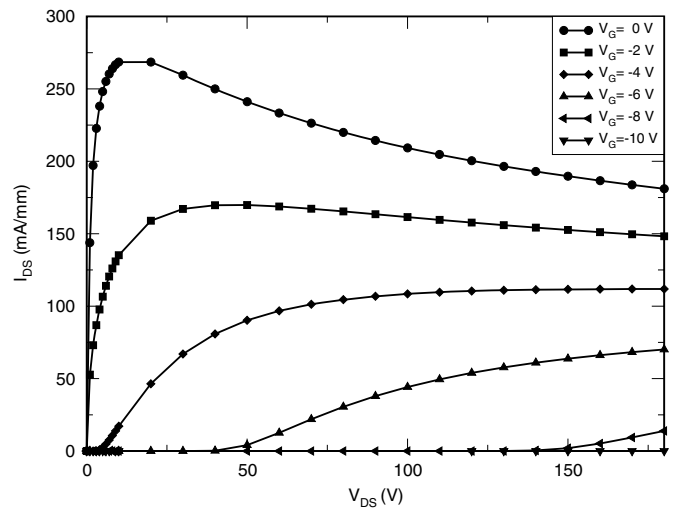


Fig. 4a. $I_{\text{DS}}-V_{\text{DS}}$ characteristics of the GaN SIT with a doping of $1 \times 10^{17} \text{ cm}^{-3}$ and source length of $2a = 0.5 \mu\text{m}$ for gate voltages noted in the figure with the temperature model described in the text turned on.

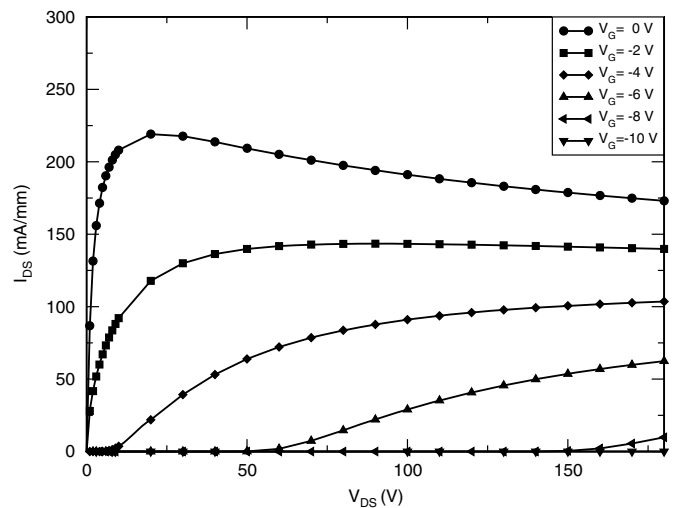


Fig. 4b. $I_{\text{DS}}-V_{\text{DS}}$ characteristics of the $\text{Al}_{0.1}\text{Ga}_{0.9}\text{N}$ SIT with a doping of $1 \times 10^{17} \text{ cm}^{-3}$ and source length of $2a = 0.5 \mu\text{m}$ for gate voltages noted in the figure with the temperature model described in the text turned on.

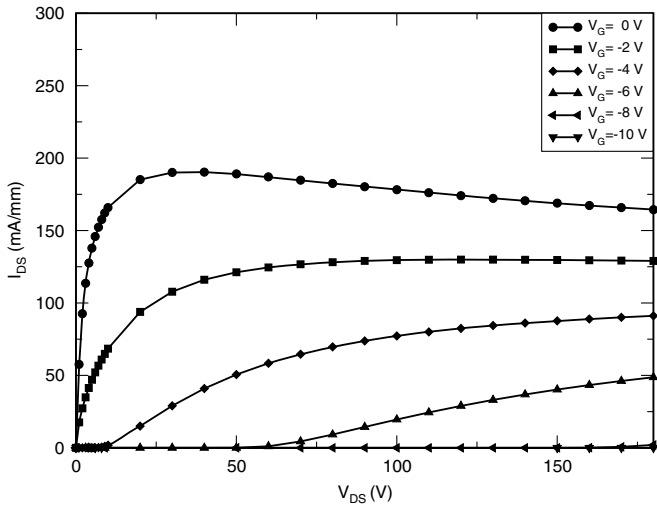


Fig. 4c. I_{DS} - V_{DS} characteristics of the $Al_{0.2}Ga_{0.8}N$ SIT with a doping of $1 \times 10^{17} \text{ cm}^{-3}$ and source length of $2a = 0.5 \mu\text{m}$ for gate voltages noted in the figure with the temperature model described in the text turned on.

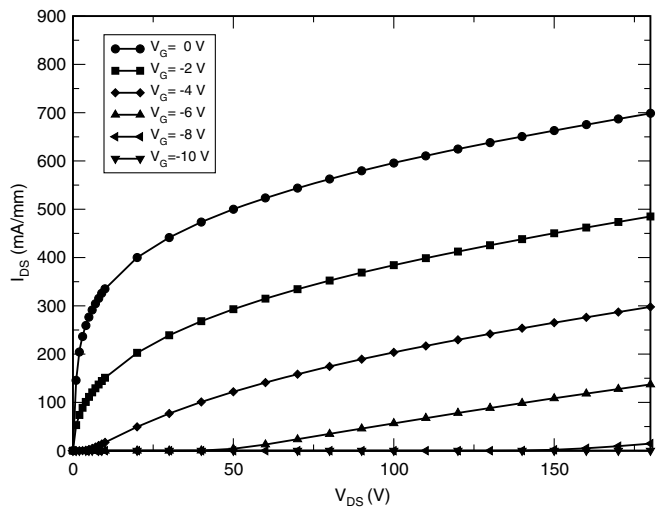


Fig. 4d. I_{DS} - V_{DS} characteristics of the GaN SIT for gate voltages noted in the figure at a constant set temperature of 300 K, an ionized impurity concentration of $1 \times 10^{17} \text{ cm}^{-3}$ and source length of $2a = 0.5 \mu\text{m}$.

with the mole fraction of aluminum is due to the increase in the V_{DS} needed for the maximum I_{DSS} biasing condition. From these temperatures, the range of duty-cycles for which the devices will be operational can be estimated.

The range of thermal variation observed within the devices was approximately 10 K for the 5% pulse condition, indicating that the temperature variation within the simulated active device region will be limited. This limited variation in temperature can be attributed to the large thermal resistance of the heat sink and the small dimensions of the active area.

It needs to be noted that the temperature during the pulse itself will show a transient increase. As compared to the average values reported here, the temperature in the device active area will be lower at the beginning of the pulse and higher at the end of the pulse. The pulse time

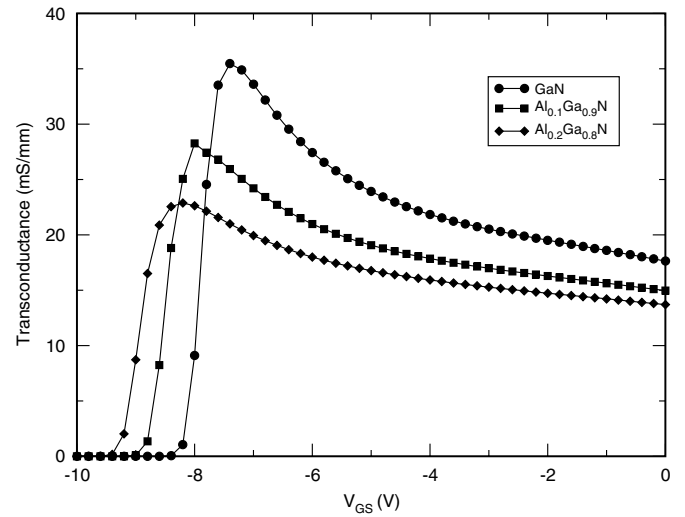


Fig. 5a. g_m - V_{GS} characteristics for the GaN, $Al_{0.1}Ga_{0.9}N$, and $Al_{0.2}Ga_{0.8}N$ SITs at a source length of $2a = 0.5 \mu\text{m}$ and an ionized impurity concentration of $1 \times 10^{17} \text{ cm}^{-3}$. The drain-to-source bias was $V_{DS} = 150 \text{ V}$, 210 V , and 260 V for the GaN, $Al_{0.1}Ga_{0.9}N$, and $Al_{0.2}Ga_{0.8}N$ SIT, respectively.

will be limited by either the maximum allowable temperature change or the maximum absolute temperature during the pulse duration. This change in temperature will result in a transient change in the drain current and the output power of the device during the pulse. For purposes of estimation of RF power levels, the average values reported here provides a mean value about which this change will occur.

In Fig. 5a, the simulated transfer characteristics for the GaN, $Al_{0.1}Ga_{0.9}N$, and $Al_{0.2}Ga_{0.8}N$ SITs are shown for a source length of $2a = 0.5 \mu\text{m}$ and a channel doping of $1 \times 10^{17} \text{ cm}^{-3}$. The drain-to-source bias, set to the quiescent bias voltage for maximum power RF operation was

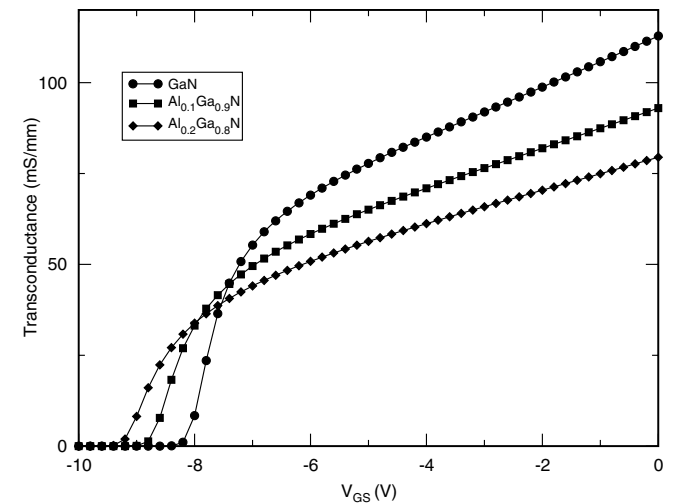


Fig. 5b. g_m - V_{GS} characteristics for the GaN, $Al_{0.1}Ga_{0.9}N$, and $Al_{0.2}Ga_{0.8}N$ SITs at a constant set temperature of 300 K, a source length of $2a = 0.5 \mu\text{m}$ and an ionized impurity concentration of $1 \times 10^{17} \text{ cm}^{-3}$. The drain-to-source bias was $V_{DS} = 150 \text{ V}$, 210 V , and 260 V for the GaN, $Al_{0.1}Ga_{0.9}N$, and $Al_{0.2}Ga_{0.8}N$ SIT, respectively.

$V_{DS} = 150$ V, 210 V, and 260 V for the GaN, $\text{Al}_{0.1}\text{Ga}_{0.9}\text{N}$, and $\text{Al}_{0.2}\text{Ga}_{0.8}\text{N}$ SITs, respectively. Fig. 5b shows the transfer characteristics for the same devices simulated at a fixed temperature of 300 K. From the comparison of Figs. 5a and 5b, we can conclude that gradual increase, up to the peak at around $V_G = -8$ V, of transconductance with decreasing gate bias seen in Fig. 5a is due to the reduction of self-heating effects with decreasing gate bias. The comparison of Figs. 5a and 5b also implies that for RF operation, the g_m - V_{GS} characteristics will exhibit the variation seen in Fig. 5b.

3.2. Effect of incorporation of AlGaN

The simulation results shown in Figs. 4a–4c indicate that I_{DSS} decreases with increasing aluminum mole fraction. This expected behavior results from the lower mobility employed for the velocity-field characteristics of the AlGaN alloys. The difference in I_{DSS} between GaN and $\text{Al}_{0.2}\text{Ga}_{0.8}\text{N}$ is about 17%. Because of the smaller drain-current, the self-heating effects observed in the static I_{DS} - V_{DS} curves are less pronounced in the simulated AlGaN devices. Similarly, from Figs. 5a and 5b, it is seen that the AlGaN alloys have lower transconductance value due to the reduction in I_{DSS} .

The high breakdown voltage attainable is a major advantage of the SIT geometry. Comparison of the I_{DS} - V_{DS} curves with impact-ionization turned on and off reveals that the breakdown is related to impact ionization. The breakdown voltages obtained using the criteria described in the previous section are 320 V, 440 V, and 520 V for the GaN, $\text{Al}_{0.1}\text{Ga}_{0.9}\text{N}$, and $\text{Al}_{0.2}\text{Ga}_{0.8}\text{N}$ SITs, respectively. For devices intended for low-frequency power-switching applications, the breakdown voltage can be increased using lower doping. In simulations using the same geometry in Fig. 3, but with a source width of $2a = 1.0$ μm and channel doping of 5×10^{16} cm^{-3} , the breakdown voltage was about 700 V for the GaN SIT and 1200 V for the $\text{Al}_{0.2}\text{Ga}_{0.8}\text{N}$ SIT. The breakdown voltages reported here ignore possible problems related to the high threading dislocation density observed in hetero-epitaxial growth, but provide estimates for the limits of capabilities of the GaN material. In particular, the simulation results indicate that the breakdown voltages obtainable with the GaN SIT may be comparable to SiC SIT, [6,7] and still higher values may be obtained with the use of AlGaN.

Fig. 6a shows the impact ionization density as a function of position in the GaN SIT at $V_{GS} = -10$ V and $V_{DS} = 320$ V, close to the breakdown of the device. As can be seen from Fig. 6a, the impact ionization is concentrated under the source close to the drain. Fig. 6b compares the impact ionization rates for the GaN, $\text{Al}_{0.1}\text{Ga}_{0.9}\text{N}$, and $\text{Al}_{0.2}\text{Ga}_{0.8}\text{N}$ SITs investigated at the same bias conditions along the center of symmetry of the device. For these simulations, the source lengths were $2a = 0.5$ μm and the channel doping was 1×10^{17} cm^{-3} . The devices employing AlGaN exhibit a much lower impact ionization rate, which in turn trans-

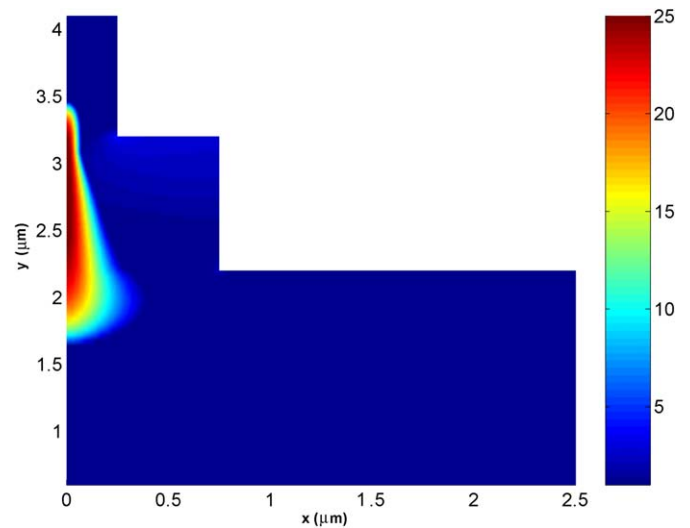


Fig. 6a. Impact ionization density in GaN SIT for $V_{DS} = -320$ V, $V_{GS} = -10$ V.

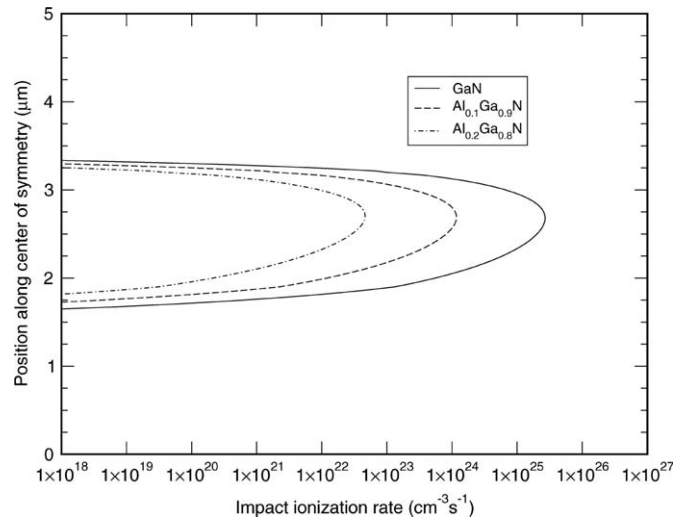


Fig. 6b. Comparison of impact ionization density for GaN, $\text{Al}_{0.1}\text{Ga}_{0.9}\text{N}$, and $\text{Al}_{0.2}\text{Ga}_{0.8}\text{N}$ SITs of ionized impurity concentration 1×10^{17} cm^{-3} along the center of symmetry.

lates to a higher breakdown voltage. This is due to the lower impact ionization rates given by the impact ionization model for AlGaN.

Fig. 7 shows the gate current of the GaN and $\text{Al}_{0.2}\text{Ga}_{0.8}\text{N}$ SITs devices at a bias of $V_{GS} = -10$ V as a function of V_{DS} . Again, the source lengths were $2a = 0.5$ μm and the channel doping was 1×10^{17} cm^{-3} . From this figure, it is seen that another advantage of the AlGaN SIT is the lower gate current that results from the lower impact-ionization rate. From Fig. 7, it is observed that the AlGaN SIT has about five orders of magnitude lower gate current density. This difference in gate currents may enable the AlGaN SIT to have a larger power-added-efficiency and higher current-gain. This result, of course, ignores possible technological problems with the preparation of high-quality Schottky contacts on etched surfaces.

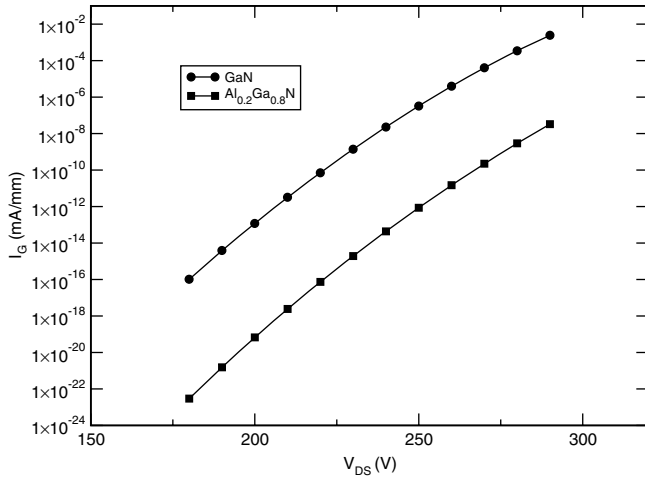


Fig. 7. Gate current for GaN and $\text{Al}_{0.2}\text{Ga}_{0.8}\text{N}$ SITs at gate-to-source bias of -10 V and different drain-to-source biases. The channel doping was $1 \times 10^{17} \text{ cm}^{-3}$ and source length of $2a = 0.5 \mu\text{m}$.

3.3. Variation of device characteristics with doping and source length

The maximum current density I_{DSS} , the knee voltage, and the output resistance were extracted from the results shown in Fig. 4. The breakdown voltage was extracted by additional simulations that compare the current levels

with and without impact ionization as described earlier. The results are tabulated in Table 4a for different values of source length, and in Table 4b for different doping levels.

The variations of the listed quantities depending on the control variable observed in Tables 4a and 4b exhibit the expected behavior with the exception of the dependence of knee voltage on the source length. The results summarized in Table 4a indicate that the knee voltage decreases with increasing source length, which can be explained by considering the negative differential resistance induced by the self-heating effects.

The results summarized in Tables 4a and 4b indicate the range of values obtainable for the GaN and AlGaN based SIT devices. It is seen that, even with limited optimization using only two of the many device parameters the device parameters can be tuned across a large range.

3.4. Analysis of expected power capability

Using the results presented in Tables 4a and 4b, estimation of the RF output power obtainable using the GaN and AlGaN SIT devices was made. Table 5 shows the estimated maximum available power per unit gate width and the optimum load impedances needed at the output of the transistor. Table 5 also shows the estimates for short-circuit unity current-gain cut-off frequency (f_{T}) obtained using the transconductance values given by the simulations and

Table 4a

Comparison of the DC transfer characteristics for different source lengths

	GaN			$\text{Al}_{0.1}\text{Ga}_{0.9}\text{N}$			$\text{Al}_{0.2}\text{Ga}_{0.8}\text{N}$		
Half source length $2a$ (μm)	0.2	0.25	0.3	0.2	0.25	0.3	0.2	0.25	0.3
Knee voltage (V)	70	10	8	110	20	14	140	28	18
Maximum zero gate-bias current (mA/mm)	114	268	430	92	220	364	78	190	320
Maximum blocking voltage (V)	300	320	340	420	440	460	500	520	540
Transconductance (g_{m0}) [mS/mm]	–	23.7	16.1	–	19.7	13.8	–	18.1	12.9

The values given were extracted from simulation results using a channel doping of $1 \times 10^{17} \text{ cm}^{-3}$.

Table 4b

Comparison of DC transfer characteristics for two different doping levels at a source length of $2a = 0.5 \mu\text{m}$

	GaN		$\text{Al}_{0.1}\text{Ga}_{0.9}\text{N}$		$\text{Al}_{0.2}\text{Ga}_{0.8}\text{N}$	
Channel doping (cm^{-3})	1×10^{17}	2×10^{17}	1×10^{17}	2×10^{17}	1×10^{17}	2×10^{17}
Knee voltage (V)	10	5	20	8	28	10
Maximum current (mA/mm)	268	744	220	631	190	558
Maximum blocking voltage (V)	320	240	440	340	520	400
Transconductance (g_{m0}) [mS/mm]	23.7	22.2	19.7	18.7	18.1	17.6

The values for a doping of 5×10^{16} are not given since the device was at cut-off at a gate bias of -2 V.

Table 5

Estimated values relevant to the RF operation of the SIT devices studied

Material	V_{B} (V)	V_{knee} (V)	I_{DSSmax} (mA/mm)	P_{o} (W/mm)	R_{L} (k Ω mm)	C_{GS} (fF)	g_{m} (mS/mm)	f_{T} (GHz)
GaN	320	10	268	10.39	1.157	0.43	23.7	8.8
$\text{Al}_{0.1}\text{Ga}_{0.9}\text{N}$	440	20	220	11.55	1.909	0.43	19.7	7.3
$\text{Al}_{0.2}\text{Ga}_{0.8}\text{N}$	520	28	190	11.69	2.589	0.43	18.1	6.7

The results are for devices with source length $0.5 \mu\text{m}$ and a channel doping of $1 \times 10^{17} \text{ cm}^{-3}$.

Table 6
All output power, P_o , calculations are made to have maximum linearity (Class A amplifier)^a

Material	V_B (V)	V_{knee} (V)	I_{DSSmax} (mA/mm)	P_o (W/mm)	P_T (W)	R_L (k Ω mm)	f_T (GHz)
HEMT (Ref. [1])	50	8	1100	5.78	22	0.038	50
HEMT (Ref. [3])	170	2.5	1200	25.1	431	0.141	22
GaN	320	10	268	10.39	1202	1.157	8.8
Al _{0.1} Ga _{0.9} N	440	20	220	11.55	2205	1.909	7.3
Al _{0.2} Ga _{0.8} N	520	28	190	11.69	3027	2.589	6.7

^a Also total power, P_T , is determined by considering the limit of 10 Ω minimum output resistance.

the estimate for C_{GS} [16]. As can be seen from Table 5, with increasing Al mole fraction of Al_xGa_{1-x}N SIT, the maximum zero-gate-voltage drain current, cut-off-frequency and transconductance decrease, whereas the breakdown voltage and optimum load resistance increase. For instance, as compared to the GaN SIT, the Al_{0.2}Ga_{0.8}N SIT has a breakdown voltage that is 60% higher but a maximum drain current that is 30% lower. Hence, the maximum output power and the optimum load resistance values are increased for Al_{0.2}Ga_{0.8}N SIT from 10.4 to 11.7 W/mm and 1.157 to 2.589 k Ω mm, respectively. As a result, we conclude that it will be possible to obtain higher total output power using Al_xGa_{1-x}N SITs. It also needs to be mentioned that, the values for power per unit gate width reported in Table 5 are similar to the values reported for SiC SITs but lower than the power densities obtained with AlGaIn/GaN HEMT [1–3].

A comparison of the SIT devices with AlGaIn/GaN HEMTs reported in the literature is given in Table 6. When maximum power output capacity is considered, the limitations of the devices due to the output resistance imposed by matching requirements must be taken into account [16]. As compared with the results of AlGaIn/GaN HEMTs reported in the literature, the GaN SIT has about 30 times larger optimum load resistance, and comparable power per unit gate width [2,3]. Thus, using the SIT structure, it is in principle possible to obtain significantly higher total output power. It needs to be noted that, the use of a field plate enables AlGaIn/GaN HEMTs to operate at higher biases, thus increasing the power density [1] and the optimum load resistance. Still, as compared to the AlGaIn/GaN HEMT with a field plate, the GaN SIT has about 8 times higher optimum load resistance and about 1/3 the power per unit gate width, implying again that the GaN SIT can deliver higher total power. The advantages of the SIT structure increase with the use of AlGaIn because AlGaIn SITs provide both higher output resistance and maximum output power. Higher output resistance of AlGaIn SITs enable the matching of wider transistors to a given load, hence increasing the total power that can be delivered. It is observed that, AlGaIn SITs offer more total output power at the expense of lower cut-off frequency.

4. Conclusions

The results presented indicate that GaN SIT devices will have breakdown voltage, current density, and RF power

density similar to those of SiC SIT and that with the use of AlGaIn the breakdown voltage can be increased further.

For RF power operation, the GaN and AlGaIn SIT can provide an f_T of about 7–8 GHz. At these frequencies, the output power density obtainable is similar to that of AlGaIn/GaN HEMTs. Within its frequency rate, the SIT structure provides an advantage for the design of high power amplifiers due to the very large output resistance. Thus, the total device width can be increased, enabling higher output power; and the optimum load resistance will still be high so that the load impedance can be easily matched with the device. This is achieved at the expense of lower operational frequencies.

Acknowledgements

The authors would like to thank Prof. Bulutay for making available the velocity-field results from his work cited in Ref. [14].

References

- [1] Wu YF, Saxler A, Moore M, Smith RP, Sheppard S, Chavarkar PM, et al. IEEE Electron Dev Lett 2004;25:117.
- [2] Lee JW, Kumar V, Schwindt R, Kuliev A, Birkhahn R, Gotthold D, et al. Electron Lett 2004;40:80.
- [3] Green B, Tilak V, Lee S, Kim H, Smart JA, Webb KJ, et al. IEEE Trans Microwave Theory Tech 2001;49:2486.
- [4] Moustakas TD, Dunham ST, Gabriela EB. MRS Int J Nitride Semicond Res 1999;4S1:G6.41.
- [5] Eastman LF. 10th Quarterly report MURI contract no. N00014-96-1-1223, 1998.
- [6] Sung YM, Casady JB, Dufrene JB, Agarwal AK. Solid-State Electron;46:605.
- [7] Henning JP, Przdacka A, Melloch MR, Cooper JA. IEEE Trans Electron Dev 2000;21:578.
- [8] Fischer C, Habas P, Heinrichsberger O, Kosina H, Lindorfer P, Pichler P, et al. MINIMOS 6 User's guide. Institut für Mikroelektronik, Technische Universität Wien, Austria, 1994.
- [9] Bougrov V, Levinshtein ME, Rumyantsev SL, Zubrilov A. Properties of advanced semiconductor materials GaN, AlN, InN, BN, SiC, SiGe. In: Levinshtein ME, Rumyantsev SL, Shur MS, editors. New York: John Wiley & Sons, Inc.; 2001. p. 1–30.
- [10] Guo Q, Yoshida A. Jpn J Appl Phys 1994;33 part 1 5A: 2453.
- [11] Popovici G, Morkoç H, Mohammad SN. In: Gil B, editor. Group III Nitride semiconductor compounds: physics and applications. Oxford: Clarendon Press; 1998. p. 16.

- [12] Sichel EK, Pankove JI. *Phys Chem Solids* 1977;38:330.
- [13] Suzuki M, Uenoyama T, Yanase A. *Phys Rev B* 1995;52: 8132.
- [14] Bulutay C. *Semicond Sci Technol* 2002;17:L59.
- [15] Farahmand M, Garetto C, Bellotti E, Brennan KF, Goano M, Ghillino E, et al. *IEEE Trans Electron Dev* 2001;48:535.
- [16] Peter HL. *MMIC design: GaAs FETs and HEMTs*. Norwood, MA: Artech House; 1989 [Chapter 6].